Modelling the Frequency-Dependent Effective Excess Charge Density in Partially Saturated Porous Media

Santiago Solazzi, Luong Duy Thanh, Kayian Hu, Damien Jougnot

Modelling the Frequency-Dependent Effective Excess Charge Density in Partially Saturated Porous Media

Santiago G. Solazzi[1], Luong Duy Thanh[2], Kayian Hu[3], and Damien Jougnot[4]

[1]Institute of Earth Sciences, University of Lausanne, CH-1015 Lausanne, Switzerland
[2]Thuyloi University, 175 Tay Son, Dong Da, Hanoi, Vietnam
[3]Department of Geophysics, School of Earth and Space Sciences, Peking University, 100871 Beijing, China
[4]Sorbonne Université, CNRS, EPHE, UMR 7619 METIS, Paris, France

Key Points:

- We present a novel flux-averaging approach to compute the dynamic effective excess charge density in partially saturated porous media.
- The model accounts for the pore size distribution of the medium and permits to estimate the dynamic electrokinetic coupling coefficient.
- The proposed approach has an excellent capability for reproducing previous models and experimental measurements in the literature.

Corresponding author: Santiago G. Solazzi, Santiago.Solazzi@unil.ch

Abstract

In the context of seismoelectric and self-potential surveying, the effective excess charge density and the electrokinetic coupling coefficient are key parameters relating the measured electrical potential and the hydraulic characteristics of the explored porous media. In this work, we present a novel flux averaging approach that permits to estimate the frequency-dependent effective excess charge density in partially saturated porous media. For this, we conceptualize the porous medium as a partially saturated bundle of capillary tubes under oscillatory flux conditions. We account for the pore size distribution (PSD) to determine the capillary-pressure saturation relationship of the corresponding medium, which, in turn, permits to determine the pore scale saturation. We then solve the Navier-Stokes equations within the saturated capillaries and, by means of a flux-averaging procedure, obtain upscaled expressions for: (i) the effective excess charge density, (ii) the effective permeability, and (iii) the electrokinetic coupling coefficient, which are functions of the saturation and the probing frequency. We analyze and explain the characteristics of these functions for three different PSDs: fractal, lognormal, and double lognormal. It is shown that the PSD characteristics have a strong effect on the corresponding electrokinetic response. The proposed flux-averaging approach has an excellent capability for reproducing experimental measurements and models in the literature, which are otherwise based on well-known empirical relationships. The results of this work constitute a useful framework for the interpretation of electrokinetic signals in partially saturated media.

Plain Language Summary

Seismic waves travel throughout the Earth deforming the rocks in their passage. If rocks are porous, permeable, and contain fluids in their pores, as is the case in many geological formations, the wave's passage may induce oscillatory fluid flow. Minerals composing rocks are commonly electrically charged and, thus, the flowing fluid can result in an electrical field. Interestingly, measuring this electrical field at the Earth's surface may permit to characterize the hydromechanical properties of geological formations of interest, motivating the so-called seismoelectric method. The effective excess charge that is mobilized by the fluid motion depends on the frequency content of the wave, and models exist to estimate this dependence in terms of the rock and fluid properties. However, in many scenarios in Earth sciences, rocks contain two immiscible fluid phases, such as, water and air, for which frequency-dependent effective excess charge density models based on pore-scale physics are missing in the literature. In this paper, we derive such a model and show that it is able to reproduce previous estimates and experimental data.

1 Introduction

The remote characterization of partially saturated geological formations using non-invasive techniques remains, to date, a challenging task within the field of applied and environmental geophysics. Given its inherent sensitivity to flow dynamics and pore fluid characteristics, the seismoelectric method can provide highly valuable information for studying this type of environments (Grobbe et al., 2020; Revil et al., 2015). The physical principles upon which seismoelectric prospecting is based on have been used in context of groundwater management and remediation (e.g., Dupuis et al., 2007; Han et al., 2004; Monachesi et al., 2018), exploration and production of hydrocarbons (e.g., Revil & Jardani, 2010), and CO_2 geosequestration operations (e.g., Zyserman et al., 2015). Novel approaches addressing the complex processes behind the seismic-to-electric conversion are of great interest, as they may help to better interpret seismoelectrical signatures in partially saturated environments.

The seismic-to-electric conversion occurs when a seismic wave propagates through a fluid saturated and charged porous medium, generating fluid displacements relative to the pore walls (e.g., Pride, 1994). Given that, in general, the surfaces of wet minerals composing porous rocks are electrically charged, an electrical double layer (EDL) arises within the saturating pore fluid which counterbalances the net charge present in the minerals. The EDL contains an excess of charge that is distributed in two layers: (i) the Stern layer, where charges are virtually immobile, and (ii) the diffuse layer, where charges have the capacity to move freely (e.g., Revil & Mahardika, 2013). Whenever a passing seismic wavefield induces flow, the excess charge located in the diffuse layer is dragged into motion, generating a streaming current which, in turn, results in an electrical potential distribution. The associated electrical field, which can be surveyed remotely, either at the Earth's surface or at boreholes, contains valuable information regarding the hydromechanical properties of the probed geological formation. Laboratory and borehole measurements evidence that seismoelectric signals are sensitive to, for example, the porosity and permeability of porous media (e.g., Zhu et al., 2008; Wang et al., 2015), and to salt concentration and dielectric permittivity of the saturating fluid (e.g., Zhu & Toksoz, 2013; Garambois & Dietrich, 2001). Seismoelectric signals measured in surface surveying or borehole logging have been used, for example, to explore earthquake rupture characteristics (e.g., Gao et al., 2016), to identify formation boundaries associated with lithological changes (e.g., Butler, 1996; Garambois & Dietrich, 2001), and to detect saturation changes in permeable geological formations (e.g., Thompson & Gist, 1993).

The seismoelectric conversion is traditionally modeled using of the electrokinetic coupling coefficient $C_{EK}(\omega)$, which is a frequency-dependent parameter relating the electrical potential difference (i.e., the electrical field) and the pore fluid pressure gradient driving the fluid flow. In this context, the most frequently used models to estimate $C_{EK}(\omega)$ are based on the works of: (i) Pride (1994) and (ii) Packard (1953). On the one hand, Pride's (1994) model is based on volume averaging principles and on the dynamic permeability model proposed by Johnson et al. (1987). On the other hand, the pioneering model of Packard (1953) considers a capillary tube of a unique radius and computes the streaming potential difference associated with an oscillatory flux. This model has been widely applied to porous media with a certain success (e.g., Reppert, 2001). Recently, Thanh et al. (2021) extended the work of Packard (1953) to take into account different pore size distributions (PSD), thus showing the effects of the porous structure on $C_{EK}(\omega)$. An alternative approach for studying the seismoelectric conversion is to compute the excess charges that are effectively dragged in the diffuse layer, that is, the effective excess charge density $\hat{Q}_\nu$, which can be subsequently used to estimate C_{EK} (e.g., Jackson, 2010; Jougnot et al., 2012; Revil & Mahardika, 2013). In the literature, many studies were performed considering this effective excess charge density but neglecting its frequency-dependence, that is, considering its low-frequency limit (e.g., Jougnot et al., 2013; Rosas-Carbajal et al., 2020). Recently, Jougnot and Solazzi (2021) extended the definition of $\hat{Q}_\nu$ to the entire frequency range $\hat{Q}_\nu(\omega)$, thus allowing to compute $C_{EK}(\omega)$. For this, the authors integrated the charges that are effectively dragged along individual pores across the probed medium, accounting for inertial effects associated with the oscillatory pressure forcing generated by a passing seismic wavefield. We remark that the latter work reconciled both Pride (1994) and Packard (1953) approaches by integrating flux averaging principles and the dynamic permeability concept. All of the above described works deal with the frequency-dependence of the coupling coefficient $C_{EK}(\omega)$ and/or the effective excess charge $\hat{Q}_\nu(\omega)$ under fully saturated conditions and, thus, modifications are needed if one wishes to employ the corresponding approaches in partially saturated porous media.

Evidence indicates conclusively that water content variations in porous media have preeminent effects on the associated seismoelectric signatures (e.g., Bordes et al., 2015; Zyserman et al., 2017). When exploring partially saturated media using the seismoelectric method, one can also use either the coupling coefficient C_{EK} and/or the effective excess charge density $\hat{Q}_\nu$ to study the electro-kinetic process. Warden et al. (2013) extended the electrokinetic coupling coefficient $C_{EK}(S_w)$ definition to address partially saturated conditions, highlighting the key influence of water content on the seismoelectric conversion. The coupling coefficient in partially saturated conditions is generally obtained by scaling its fully saturated counterpart by the wetting phase saturation (Bordes et al., 2015; Revil & Mahardika, 2013; Warden et al., 2013; Zyserman et al., 2017). Later on, Revil and Mahardika (2013) proposed a simple model to compute the saturation- and frequency-dependent effective excess charge density of partially saturated porous media $\hat{Q}_\nu(\omega, S_w)$ and through it, to estimate $C_{EK}(\omega, S_w)$. For this, Revil and Mahardika (2013) rely on concept of dynamic permeability, using a Debye approximation, and on empiric and broadly used scaling laws, thus extending the approach proposed by Pride (1994) to partially saturated media. As far as we know, to date, a model deriving the saturation- and frequency-dependent effective excess charge density $\hat{Q}_\nu(\omega, S_w)$ from first principles, that is, from flux averaging the pore scale physics, is lacking in the specific literature. Such derivation is of fundamental importance, as it would permit to: (i) couple flux, electrokinetic properties, and the pore size distribution characteristics of porous media; (ii) validate the approach proposed by Revil and Mahardika (2013).

In this work, we propose a novel flux averaging approach to estimate the effective excess charge density as a function of saturation and frequency $\hat{Q}_\nu(\omega, S_w)$. The paper is structured as follows. First, we resume the theory behind the frequency-dependence of the effective excess charge density $\hat{Q}_\nu(\omega)$ and other parameters, such as, the dynamic permeability $\kappa(\omega)$ and the electrokinetic coupling coefficient $C_{\mathrm{EK}}(\omega)$. Then, we propose a model to account for different saturation states in the latter. We evaluate the saturation and frequency response of the medium considering fractal, lognormal, and double lognormal PSDs. Finally, we compare the proposed approach with the model proposed by Revil and Mahardika (2013) and with published experimental data.

2 Theory

In this section, we resume the theory of dynamic (frequency-dependent) permeability and effective excess charge density in fully saturated media. Then, we extend these definitions to the partially saturated state, considering that the pore fluids are immiscible and that their distribution throughout the pore space is determined by capillary forces. In the case of the dynamic permeability, we follow the work of Solazzi et al. (2020), who derived frequency- and saturation-dependent effective permeability estimates in partially saturated porous media.

2.1 Frequency-Dependent Effective Excess Charge Density in Fully Saturated Media

2.1.1 Fluid Flow and Dynamic Permeability

Let us consider a cylindrical representative elementary volume (REV) of a porous material of length L (m) and radius R_{REV} (m). We conceptualize the fluid flow of a single phase across the REV using a bundle of aligned capillary tubes, oriented along the axis of the cylindrical REV, comprising radii R (m) whose sizes vary from $R_{\min}$ to $R_{\max}$. The pore-size distribution (PSD) is such that the number of capillaries with radii between R and $R+\mathrm{d}R$ is given by $\mathfrak{f}(R)\mathrm{d}R$. Note that this conceptualization of a porous medium under fluid flow is based on similar concepts as the classic model of Kozeny (1927), which is broadly used in permeable soils (e.g., Mavko et al., 2009). Let us also consider that an incompressible Newtonian fluid characterized by a shear viscosity η (Pa.s) and density ρ (kg/m^3) saturates the porous medium, whose solid matrix is assumed to be rigid (Johnson et al., 1987). Note that the fluid incompressibility assumption is valid at the pore scale as long as the wavelengths of possible acoustic waves traveling in the fluid are much larger than the characteristic pore size (Johnson et al., 1987; Zhou & Sheng, 1989). Finally, we consider that the fluid flow within the pore space is of laminar-type associated with a small Reynold's number (Auriault et al., 1985; Smeulders et al., 1992).

The REV structure is then subjected to an oscillatory pore fluid pressure difference $\Delta\hat{p} = \Delta p\, e^{-i\omega t}$ (Pa) along its axis., with ω denoting the angular frequency (rad/s). Solving the incompressible Navier-Stokes equations under the assumptions mentioned above, the fluid velocity v^f (m/s) in a capillary of internal radius $0 \leq r \leq R$ responds to (Solazzi et al., 2020)

$$v^f(r,\omega) = -\frac{1}{\tau\eta k^2}\left[\frac{J_0(kr)}{J_0(kR)} - 1\right]\frac{\Delta p}{L}, \tag{1}$$

where $k^2 = i\omega\rho/\eta$ and J_ν are Bessel functions of the first kind of order ν. The tortuosity is given by $\tau = l^*/L$, where l^* is the actual flow path length. Note that we have dropped the harmonic term $e^{-i\omega t}$ for ease of notation. Integrating equation (1) over the cross-sectional area of the pore, the corresponding volumetric flow rate (m^3/s) through a single capillary is given by (e.g., Johnson et al., 1987)

$$q(R,\omega) = -\frac{\pi R^2}{\tau\eta k^2}\left[\frac{2}{kR}\frac{J_1(kR)}{J_0(kR)} - 1\right]\frac{\Delta p}{L}. \tag{2}$$

The volumetric flow rate $Q^{\mathrm{sat}}_{\mathrm{flow}}$ (m^3/s) at the fully-saturated REV-scale can be obtained by integrating equation (2) over the entire range of pore sizes within the REV

$$Q^{\mathrm{sat}}_{\mathrm{flow}} = \int_{R_{\min}}^{R_{\max}} q(R,\omega)\,\mathfrak{f}(R)\,\mathrm{d}R. \tag{3}$$

The effective Darcy velocity at the REV scale $\mathrm{v}^{\mathrm{sat}}$ (m/s) is obtained by scaling the volumetric flow rate by the corresponding cross-sectional area, that is, $\mathrm{v}^{\mathrm{sat}} = Q^{\mathrm{sat}}_{\mathrm{flow}}/\pi R^2_{\mathrm{REV}}$.

If one increases the frequency of the oscillatory pressure forcing, a transition from viscous- to inertia-dominated flow occurs. For a given critical angular frequency ω_{c}, the viscous skin depth $\delta = \sqrt{2\eta/\rho\omega}$ (m) becomes comparable to the radii of the largest saturated pores (Johnson et al., 1987)

$$\omega_{\mathrm{c}} \simeq \frac{2\eta}{\breve{R}^2\rho}, \tag{4}$$

with $\breve{R}$ being the characteristic radius of the saturated porous medium. For frequencies higher than ω_{c} the fluid motion becomes viscously decoupled. In this context, the fluid flow and the underlying fluid pressure forcing become out of phase and the fluid flow amplitude decreases.

The dynamic (frequency-dependent) permeability $\kappa(\omega)$ (m^2) is then computed using Darcy's law, that is, relating the fluid flow and the pressure gradient along the REV (Solazzi et al., 2020)

$$\kappa(\omega) = \frac{1}{\tau R^2_{\mathrm{REV}} k^2}\int_{R_{\min}}^{R_{\max}}\left[\frac{2}{kR}\frac{J_1(kR)}{J_0(kR)} - 1\right] R^2\mathfrak{f}(R)\,\mathrm{d}R. \tag{5}$$

Equation (5) can be solved numerically provided that $\mathfrak{f}(R)$, $R_{\min}$, and $R_{\max}$ are known. One of the consequences of equation (5) is that the pore size distribution has an impact on the dynamic permeability characteristics, such as, the value of ω_c (Solazzi et al., 2020).

We remark that, following a different approach than the one proposed by Solazzi et al. (2020), Li et al. (2021) arrived to the very same conclusion.

The low-frequency limit of equation (5) is the (Poiseuille-type) permeability of the medium (Blunt, 2017)

$$\kappa^0 = \frac{1}{\tau 8 R_{\mathrm{REV}}^2} \int_{R_{\min}}^{R_{\max}} R^4 \mathfrak{f}(R)\, \mathrm{d}R. \tag{6}$$

2.1.2 Effective Excess Charge Density

Let us now consider that the capillaries of the previously described porous medium are saturated by a binary symmetric electrolyte (e.g., NaCl) with ionic concentration C_i^w ($\mathrm{mol\,m^{-3}}$) and valence $z_i = \pm 1$, with i denoting the considered ion. Minerals composing the pore walls of rocks normally exhibit surface charges when in contact with water. As an example, silicate and aluminosilicate minerals present negative charges under natural conditions. Let us then denote co-ions the ions that present the same charge as the minerals constituting the pore walls (e.g., Cl^-) and, counter-ions those charged with an opposite valence (e.g., Na^+). For the system to be electrically neutral, surface charges are balanced by an excess charge in the pore water. The latter are distributed in the EDL. Within the EDL, the diffuse layer comprises co-ions and counter-ions that are able to move and, also, is characterized by a net excess of charge. Hereafter we consider that the shear plane, that is, the plane that separates the stationary fluid and the moving fluid, corresponds to the interface between the Stern layer and the diffuse layer. The electrical potential along this plane is referred to as Zeta potential.

The distribution of the excess charges in the diffuse layer within a single capillary is governed by the Poisson-Boltzmann equation

$$\nabla^2 \varphi\,(r) = -\frac{\overline{Q}_\nu\,(r)}{\varepsilon_r \varepsilon_0}, \tag{7}$$

where $\varphi(r)$ (V) is the electric potential and $\overline{Q}_\nu(r)$ ($\mathrm{C\,m^{-3}}$) is the excess charge density in the liquid at a distance $0 \leq r \leq R$ from the pore-centre. The relative permittivity of the fluid and the dielectric permittivity of vacuum are given by ε_r and $\varepsilon_0 = 8.854 \times 10^{-12}\,\mathrm{F\,m^{-1}}$, respectively. Under the above conditions, the effective charge density responds to (e.g., Jougnot et al., 2012)

$$\overline{Q}_\nu\,(r) = N_A e_0 C_{NaCl}^w \left[e^{\left(-\frac{e_0 \varphi(r)}{k_B T}\right)} - e^{\left(\frac{e_0 \varphi(r)}{k_B T}\right)} \right]. \tag{8}$$

Generally, equation (7) is solved assuming: (i) a Debye-Hückel linear approximation, that is, $e_0\varphi(r)/k_BT << 1$; (ii) that the pore size is considerably larger than thickness of the double layer. In this context, the two exponential terms in Eq. (8) can be expressed through the sinh function and, then, one can make use of the fact that for sufficiently small arguments the sinh function tends to its corresponding argument, that is, $\sinh\left[e_0\varphi(r)/k_BT\right] \simeq e_0\varphi(r)/k_BT$. Consequently, the electric potential is given by

$$\varphi(r) = \zeta e^{\frac{r-R}{l_D}}, \tag{9}$$

where l_D is the Debye length characterizing the electrical double layer thickness given by

$$l_D = \sqrt{\frac{\varepsilon_0\varepsilon_r k_B T}{2N_A e_0^2 C_{NaCl}^w}}. \tag{10}$$

The dependence of the ζ potential on the ionic concentration is hereby estimated following (Pride & Morgan, 1991)

$$\zeta(C_{NaCl}^w) = a + b\log_{10}(C_{NaCl}^w). \tag{11}$$

The fitting parameters a and b are taken as $a = -6.43$ mV and $b = 20.85$ mV, as estimated by (Jaafar et al., 2009) for NaCl brine and silicate-based materials.

In this context, the effective excess charge density $\hat{Q}_\nu^R$ carried by the water flow in a single capillary of radius R responds to (Jougnot & Solazzi, 2021)

$$\hat{Q}_\nu^R(\omega) = \frac{\int_0^R \overline{Q}_\nu(r) v^f(r,\omega) r\mathrm{d}r}{\int_0^R v^f(r,\omega) r\mathrm{d}r}. \tag{12}$$

The effective excess charge density $\hat{Q}_\nu^R$ is different from the simple excess charge density $\bar{Q}_\nu$, since $\hat{Q}_\nu^R$ is the excess charge that is effectively dragged by the water flow, which is smaller than the total amount of excess charge present in the diffuse layer ($\bar{Q}_\nu : \bar{Q}_\nu >> \hat{Q}_\nu^R$). For further details on this particular topic, we refer the readers to the discussion sections of Jougnot et al. (2019, 2020).

The effective excess charge carried by the water flow in the fully saturated REV can be obtained by integrating $\hat{Q}_\nu^R(\omega)$, weighted by the corresponding fluxes, over the entire range of pore sizes

$$\hat{Q}_\nu^{\mathrm{sat,REV}}(\omega) = \frac{\int_{R_{\min}}^{R_{\max}} \hat{Q}_\nu^R(\omega) q(R,\omega)\mathfrak{f}(R)\,\mathrm{d}R}{\int_{R_{\min}}^{R_{\max}} q(R,\omega)\mathfrak{f}(R)\,\mathrm{d}R}, \tag{13}$$

where $q(R,\omega)$ is the volumetric flow rate through a single capillary of radius R given by equation (3). We remark that the supra-index "sat" denotes that the medium is fully saturated and helps to discriminate this parameter from its partially saturated counterpart, defined in the next subsection of this paper.

Finally, based on the above described expressions, it is possible to define a relative excess charge density (Jougnot & Solazzi, 2021),

$$\hat{Q}_{\nu}^{\mathrm{sat,rel}}(\omega) = \frac{\hat{Q}_{\nu}^{\mathrm{sat,REV}}(\omega)}{\hat{Q}_{\nu}^{\mathrm{sat,\,0}}}, \tag{14}$$

where $\hat{Q}_{\nu}^{\mathrm{sat,\,0}} = \lim_{\omega\to 0} \hat{Q}_{\nu}^{\mathrm{sat,REV}}(\omega)$ is the steady-state (low frequency) excess charge density of the fully saturated medium.

2.1.3 Electrokinetic Coupling Coefficient

At the REV scale, the electrokinetic coupling is usually quantified by means of the electrokinetic coupling coefficient (e.g., Jaafar et al., 2009)

$$C_{EK}(\omega) = \left(\frac{\partial \varphi}{\partial p}\right)_{\mathbf{J}=\mathbf{0},\,\ddot{\mathbf{u}}_s=0} = \frac{\Delta V}{\Delta p}, \tag{15}$$

which is the ratio of the electrical potential difference ΔV and the pressure difference Δp measured at the boundaries of a probed rock sample in the absence of total current densities $\mathbf{J} = \mathbf{0}$ and solid frame accelerations $\ddot{\mathbf{u}}_s = 0$. Through a simple variable change, the frequency dependent coupling coefficient for a fully saturated medium can be expressed as (e.g., Jougnot et al., 2020; Jougnot & Solazzi, 2021; Revil & Mahardika, 2013)

$$C_{EK}^{\mathrm{sat}}(\omega) = -\frac{\hat{Q}_{\nu}^{\mathrm{sat,REV}}(\omega)\kappa(\omega)}{\eta_w \sigma^{\mathrm{sat}}(\omega)}, \tag{16}$$

where $\kappa_w(\omega)$ and $\hat{Q}_{\nu}^{\mathrm{sat,REV}}(\omega)$ respond to equations (5) and (13), respectively. We remark here that the electrical conductivity $\sigma^{\mathrm{sat}}(\omega)$ may, as well, present a frequency dependence. For a detailed derivation of equation (16), we refer the reader to, for example, the work of Revil and Mahardika (2013) (specifically to equations 34 to 38). Note that, for steady-state conditions (low-frequency limit), Jougnot et al. (2019) showed that this equation is valid for any kind of pore space geometry (pore shape and connectivity) and that the geometrical information is carried through the permeability. In this sense, as long as the thin double layer assumption is respected, permeability effects are cancelled in the coupling coefficient as the effective excess charge density depends on the inverse of the permeability (see discussion in Jougnot et al. (2019, 2020)). However, such simplification does not hold for the whole frequency range (e.g., Jougnot & Solazzi, 2021), as the relationship between permeability and effective excess charge density is more complex when considering frequency-dependent effects (see equation 13).

The relative electrokinetic coupling coefficient can be expressed as (Jougnot & Solazzi, 2021)

$$C_{EK}^{\mathrm{sat,\,rel}}(\omega) = \frac{C_{EK}^{\mathrm{sat}}(\omega)}{C_{EK}^{\mathrm{sat,\,0}}}, \tag{17}$$

where $C_{EK}^{\mathrm{sat,\,0}} = \lim_{\omega\to 0} C_{EK}^{\mathrm{sat}}(\omega)$ is the steady-state electrokinetic coupling coefficient of the fully saturated medium.

2.2 Frequency-Dependent Effective Excess Charge Density in Partially Saturated Media

2.2.1 Fluid Flow and Effective Dynamic Permeability

In the context of fluid flow in partially saturated porous media, the wetting phase flows through a fraction of the corresponding medium. Thus, Darcy's equation in partially-saturated media is (e.g., Bear, 1972)

$$\mathbf{v}_w = -\frac{\kappa^{\mathrm{eff}}}{\eta_w}\nabla p_w. \tag{18}$$

In equation (18), $\mathbf{v}_w$ is Darcy's velocity of the wetting phase, κ^{eff} is the effective permeability of the wetting phase which responds to

$$\kappa^{\mathrm{eff}}(\omega) = \kappa(\omega)\kappa_w^{\mathrm{rel}}(p_c,\omega), \tag{19}$$

with $\kappa_w^{\mathrm{rel}}(p_c,\omega)$ denoting the frequency dependent relative permeability of the wetting phase, and p_{c} (Pa) the capillary pressure.

The Young-Laplace equation permits us to obtain the capillary pressure in partially saturated capillary of radius R_{p} (e.g., Bear, 1972)

$$p_{\mathrm{c}} = \frac{2\gamma\cos(\beta)}{R_{\mathrm{p}}}, \tag{20}$$

where γ (N/m) is the interfacial tension and β (rad) is the contact angle between the solid walls and the saturating immiscible fluid phases. At the REV scale, p_c normally presents a functional relationship with the saturation of the medium (e.g., Van Genuchten, 1980; Brooks & Corey, 1964). If the medium is at capillary pressure equilibrium, all capillaries presenting radii $R > R_{\mathrm{p}}(p_{\mathrm{c}}) = \frac{2\gamma\cos(\beta)}{p_{\mathrm{c}}}$ are to be saturated by the non-wetting phase (e.g., Mualem, 1976) and those satisfying $R \leq R_{\mathrm{p}}(p_{\mathrm{c}})$ are to be saturated by the wetting phase. It is then straightforward to compute the associated effective wetting phase saturation $S_{\mathrm{ew}}(p_{\mathrm{c}})$, which yields (e.g., Blunt, 2017)

$$S_{\mathrm{we}}(p_{\mathrm{c}}) = \frac{\int_{R_{\min}}^{R_{\mathrm{p}}(p_{\mathrm{c}})} R^2\mathfrak{f}(R)\,\mathrm{d}R}{\int_{R_{\min}}^{R_{\max}} R^2\mathfrak{f}(R)\,\mathrm{d}R}, \quad \text{with} \quad p_{\mathrm{c,min}} \leq p_{\mathrm{c}} \leq p_{\mathrm{c,max}}, \tag{21}$$

with $p_{\mathrm{c,max}} = 2\gamma\cos\beta/R_{\mathrm{min}}$ and $p_{\mathrm{c,min}} = 2\gamma\cos\beta/R_{\mathrm{max}}$. When capillary pressures are such that $p_{\mathrm{c}} < p_{\mathrm{c,min}}$ we have $S_{\mathrm{we}} = 1$ and, alternatively, when $p_{\mathrm{c}} > p_{\mathrm{c,max}}$ we have $S_{\mathrm{we}} = 0$. We remark that equation (21) assumes that the partially saturated porous medium is characterized by fully connected fluid phases, which saturate particular subsets of the probed porous medium (Blunt, 2017). The effective saturation S_{we} is related to the total S_w saturation by $S_w = S_{\mathrm{we}}(1-S_{\mathrm{wr}})+S_{\mathrm{wr}}$, with S_{wr} denoting the wetting fluid residual saturation.

The effective volumetric flow rates for the wetting phase can be obtained by integrating equation (3) between R_{min} and $R_{\mathrm{p}}(p_{\mathrm{c}})$, respectively. Then, employing equation (18), the frequency-dependent dynamic effective permeability for the wetting phase is (Solazzi et al., 2020)

$$\kappa^{\mathrm{eff}}(p_{\mathrm{c}}, \omega) = \frac{1}{\tau R_{\mathrm{REV}}^2 k_w^2} \int_{R_{\mathrm{min}}}^{R_{\mathrm{p}}(p_{\mathrm{c}})} \left[\frac{2}{k_w R} \frac{J_1(k_w R)}{J_0(k_w R)} - 1 \right] R^2 \mathfrak{f}(R)\, \mathrm{d}R, \tag{22}$$

where $k_w^2 = i\omega\rho_w/\eta_w$. Note that equation (22) is the extension of equation (5) to partially saturated media, as $p_c = p_c(S_w)$. As expected, in the low-frequency limit, this expression converge to its Poiseuille-type counterpart (e.g., Blunt, 2017)

$$\kappa_w^{\mathrm{eff},\,0}(p_{\mathrm{c}}) = \frac{1}{\tau 8 R_{\mathrm{REV}}^2} \int_{R_{\mathrm{min}}}^{R_{\mathrm{p}}(p_{\mathrm{c}})} R^4 \mathfrak{f}(R)\, \mathrm{d}R. \tag{23}$$

Please note that, in the derivation of equation (22), a no-slip condition is assumed to prevail at the interface between the saturating fluid and the pore walls. In presence of a non-negligible flow velocity at the fluid-pore wall boundary (slip condition), which may arise due to wettability effects, the dynamic permeability estimates (Li et al., 2020) and the electrokinetic response of the medium (Collini & Jackson, 2022) are expected to change. Such boundary effects are, however, beyond the scope of this work.

2.2.2 Effective Excess Charge Density

The effective excess charge carried by the water flow a the partially saturated medium is then obtained by integrating the excess charge along the pores that are effectively saturated with water for a given capillary pressure p_c, weighted by the corresponding flow rates

$$\hat{Q}_\nu^{\mathrm{REV}}(p_c, \omega) = \frac{\int_{R_{min}}^{R_p(p_c)} \hat{Q}_\nu^R(\omega) q(R,\omega) \mathfrak{f}(R)\, \mathrm{d}R}{\int_{R_{\mathrm{min}}}^{R_p(p_c)} q(R,\omega)\mathfrak{f}(R)\, \mathrm{d}R}. \tag{24}$$

Note that since the capillary pressure p_{c} is related to the water saturation S_w, we consider $\hat{Q}_\nu^{\mathrm{REV}}(p_c(S_w), \omega) \equiv \hat{Q}_\nu^{\mathrm{REV}}(S_w, \omega)$, without loss of generality.

Notably, it is possible to define a frequency- and saturation-dependent relative excess charge density

$$\hat{Q}_\nu^{\text{rel}}(S_w,\omega) = \frac{\hat{Q}_\nu^{REV}(S_w,\omega)}{\hat{Q}_\nu^0(S_w)}, \tag{25}$$

where $\hat{Q}_\nu^0(S_w) = \lim_{\omega\to 0} \hat{Q}_\nu(S_w,\omega)$.

2.2.3 Electrokinetic Coupling Coefficient

By means of the above defined parameters, we extend the dynamic electrokinetic coupling definition to partially saturated conditions as (Revil & Mahardika, 2013)

$$C_{EK}(S_w,\omega) = -\frac{\hat{Q}_\nu^{\text{REV}}(S_w,\omega)\kappa^{\text{eff}}(S_w,\omega)}{\eta_w\sigma(S_w,\omega)}, \tag{26}$$

where $\kappa^{\text{eff}}(S_w,\omega)$ and $\hat{Q}_\nu^{\text{REV}}(S_w,\omega)$ respond to equations (22) and (24), respectively. The electrical conductivity (S/m), in its low-frequency limit, responds to (Waxman & Smits, 1968)

$$\sigma^0(S_w) = \frac{S_w^n}{F}\left(\sigma_w + \frac{\sigma_s}{S_w}\right), \tag{27}$$

where σ_s (S/m) is the surface conductivity, $F = \tau/\phi$ is the formation factor, and n the second Archie's coefficient. Even though the electrical conductivity can be considered as frequency dependent, for simplicity, we hereafter consider $\sigma(S_w,\omega) \approx \sigma^0(S_w)$. For more information about the frequency dependence of the electrical conductivity, we refer the readers to pertinent literature on the subject (e.g., Jougnot et al., 2010; Revil, 2013).

Finally, the relative electrokinetic coupling coefficient for partially saturated media responds to

$$C_{EK}^{\text{rel}}(S_w,\omega) = \frac{C_{EK}(S_w,\omega)}{C_{EK}^0(S_w)}, \tag{28}$$

where $C_{EK}^0(S_w) = \lim_{\omega\to 0} C_{EK}(S_w,\omega)$.

Equations (24) and (26) are the central methodological result of this paper, as they define the saturation- and frequency-dependent effective excess charge density and electrokinetic coupling coefficient at the REV scale by means of a flux-averaging upscaling procedure. We remark that both $\hat{Q}_\nu^{\text{REV}}(S_w,\omega)$ and $C_{EK}(S_w,\omega)$ depend on the PSD of the probed medium, a characteristic that is included in the corresponding expressions via the $\mathfrak{f}(R)$ function.

3 Results

In this section, we analyze the effects of frequency and saturation on the effective excess charge density $\hat{Q}_{\nu}^{\mathrm{REV}}(S_w,\omega)$ and the electrokinetic coupling coefficient $C_{EK}(S_w,\omega)$ in porous media. We assess the effects of the pore size distribution in the corresponding response by considering: (i) fractal, (ii) lognormal, and (iii) double-lognormal pore size distributions.

3.1 Pore Size Distribution

3.1.1 Fractal Distribution Function

As a first case, we consider a cumulative size distribution of pores whose radii are greater than or equal to R that obeys the following fractal law (e.g., Guarracino et al., 2014; Tyler & Wheatcraft, 1990; Yu et al., 2003)

$$N(R) = \left(\frac{R_{\max}}{R}\right)^{D}, \tag{29}$$

where D is the fractal dimension of the pore size with $1 < D < 2$ and $R_{\min} < R < R_{\max}$. The total number of pores, from $R_{\min}$ to $R_{\max}$, is given by

$$N_t(R_{\min}) = \left(\frac{R_{\max}}{R_{\min}}\right)^{D}. \tag{30}$$

On the other hand, differentiating $N(R)$ with respect to R, we obtain the number of pores whose radii are between R and $R + \mathrm{d}R$:

$$-\mathrm{d}N = DR_{\max}^{D}R^{-D-1}\mathrm{d}R = \mathfrak{f}(R)\mathrm{d}R. \tag{31}$$

Dividing equations (31) and (30), we obtain the probability density function $f_r(R)$

$$-\frac{\mathrm{d}N}{N_t} = DR_{\min}^{D}R^{-D-1}\mathrm{d}R = f_r(R)\mathrm{d}R, \tag{32}$$

such that,

$$\int_{R_{\min}}^{R_{\max}} f_r(R)\mathrm{d}R = 1 - \left(\frac{R_{\min}}{R_{\max}}\right)^{D} \equiv 1, \tag{33}$$

which clearly holds if $(R_{\min}/R_{\max})^{D} \simeq 0$. In this sense, the condition $R_{\max} >> R_{\min}$ must be satisfied for fractal analysis of porous media. Please note that, $\mathfrak{f}(R) = N_t f_r(R)$.

3.1.2 Lognormal Distribution Function

The lognormal distribution probability density function responds to

$$f_r(R) = \frac{1}{\mathfrak{s}R\sqrt{2\pi}} \exp\left(-\frac{(\log R - \mathfrak{x})^2}{2\mathfrak{s}^2}\right). \tag{34}$$

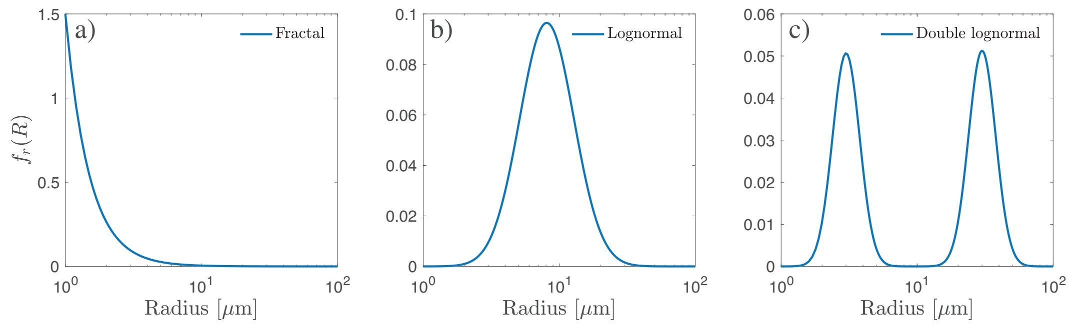

Figure 1. Probability density functions associated with the pore size distributions used in this work: (a) fractal ($D = 1.5$), (b) lognormal ($R^* = 10\,\mu$m and $\mathfrak{s} = 0.46$), and (c) double lognormal ($R_1^* = 3.1\,\mu$m, $R_2^* = 31\,\mu$m, $\mathfrak{s}_d = \mathfrak{s}/2$, $\beta_1 = 0.09$, and $\beta_2 = 0.91$).

where $\mathfrak{r} = \log R^*$ and $\mathfrak{s}$ denote the scale and shape parameters. Again, we consider that $\mathfrak{f}(R) = N_t f_r(R)$, where N_t is the total number of pores in the medium.

3.1.3 Double Lognormal Distribution Function

The double lognormal distribution can be regarded as the sum of two lognormal distributions with the same shape parameter $\mathfrak{s}_d$ and responds to

$$f_r(R) = \beta_1 \frac{1}{\mathfrak{s}_d R\sqrt{2\pi}} \exp\left(-\frac{(\log R - \mathfrak{r}_1)^2}{2\mathfrak{s}_d^2}\right) + \beta_2 \frac{1}{\mathfrak{s}_d R\sqrt{2\pi}} \exp\left(-\frac{(\log R - \mathfrak{r}_2)^2}{2\mathfrak{s}_d^2}\right), \quad (35)$$

where $\mathfrak{r}_1 = \log R_1^*$ and $\mathfrak{r}_2 = \log R_2^*$, and $\beta_1 + \beta_2 = 1$. Again, we consider that $\mathfrak{f}(R) = N_t f_r(R)$.

Figure 1 shows the representative PSDs considered in this work with pore radius ranging from 1 μm to 100 μm: (a) fractal ($D = 1.5$), (b) lognormal ($R^* = 10\,\mu$m and $\mathfrak{s} = 0.46$), and (c) double lognormal ($R_1^* = 3.1\,\mu$m, $R_2^* = 31\,\mu$m, $\mathfrak{s}_d = \mathfrak{s}/2$, $\beta_1 = 0.09$, and $\beta_2 = 0.91$). We remark that smaller pore radii dominate the response of the medium for fractal PSD, while pores distribute more evenly throughout the given radii for the lognormal and double lognormal PSDs. As shown below, the PSD characteristics result in significantly different responses for the effective permeability, the effective excess charge density, and, consequently, the electrokinetic coupling in porous media.

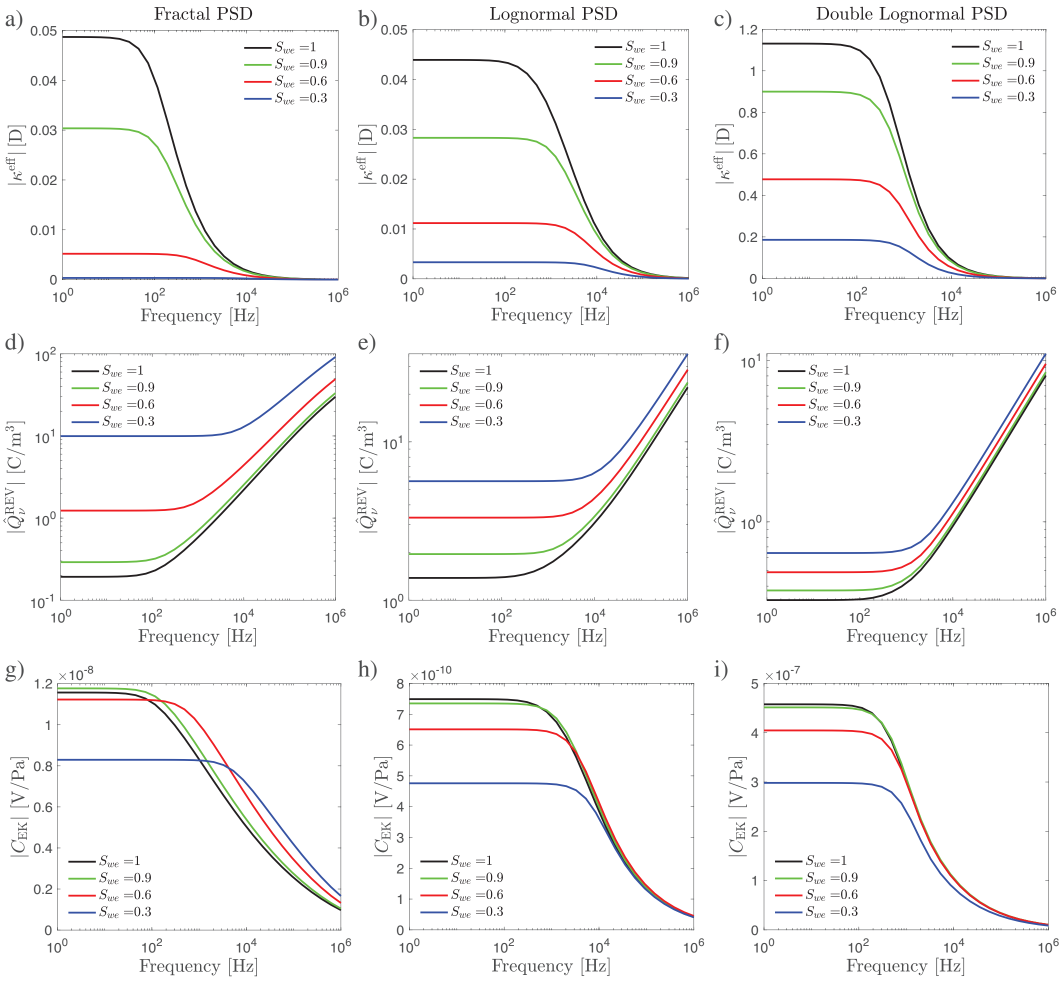

Figure 2. Absolute value of the effective dynamic permeability κ_w^{eff}, effective excess charge density $\hat{Q}_\nu^{\mathrm{REV}}$, and effective electrokinetic coupling coefficient C_{EK} as functions of frequency for different saturation states. Each row illustrates the result for a different PSD: (a, d, g) fractal ($D = 1.5$), (b, e, h) lognormal ($R^* = 10\,\mu\mathrm{m}$ and $\mathfrak{s} = 0.46$), and (c, f, i) double lognormal ($R_1^* = 3.1\,\mu\mathrm{m}$, $R_2^* = 31\,\mu\mathrm{m}$, $\mathfrak{s}_d = \mathfrak{s}/2$, $\beta_1 = 0.09$, and $\beta_2 = 0.91$).

3.2 Numerical Analysis of the Proposed Model

Let us consider three porous media represented by: (i) a fractal PSD with a dimension $D = 1.5$, (ii) a lognormal PSD characterized by $R^* = 10\,\mu\text{m}$ and $\mathfrak{s} = 0.46$, and (iii) a double lognormal PSD characterized by $R_1^* = 3.1\,\mu\text{m}$, $R_2^* = 31\,\mu\text{m}$, $\mathfrak{s}_d = \mathfrak{s}/2$, $\beta_1 = 0.09$, and $\beta_2 = 0.91$. We assume that they all have $\tau \simeq 1$, $R_{\min} = 1\ \mu\text{m}$, and $R_{\max} = 100\ \mu\text{m}$ and, also, the same total number of pores N_t, which is taken from the fractal distribution characteristics (equation 30). The pore fluid properties that saturate these probed media are summarized in Table 1.

Following Solazzi et al. (2020), we numerically solve equation (22) and obtain the saturation- and frequency-dependent effective permeability for the above described porous media. Figures 2a, 2b, and 2c illustrate the magnitude of $\kappa^{\text{eff}}(S_w, \omega)$ as a function of frequency for the three PSDs described above. Note that each column of Figure 2 is associated with one particular PSD. In this context, we plot different effective saturation states, identified by different colored lines. We observe that the absolute value of κ^{eff} decreases with frequency for $f > f_c$, with $f_c = \omega_c/2\pi$ denoting the critical frequency (Figures 2a, 2b, and 2c). Recall that f_c is determined by the PSD characteristics, specifically by the largest saturated pores of the distribution. The frequency-dependent behavior of $|\kappa^{\text{eff}}(S_w, \omega)|$ is explained by the onset of the inertia effects for $f \geq f_c$. When inertia effects prevail, the amplitude of the dynamic permeability drops and its phase increases (e.g., Zhou & Sheng, 1989). As previously observed by Solazzi et al. (2020), the critical frequency f_c increases with decreasing saturation, as water retreats to increasingly smaller pores. We also note that $|\kappa^{\text{eff}}|$ increases with water saturation. The corresponding response is modulated by the PSD of the probed porous medium. The reason behind this behavior is that the overall number of pores saturated by water decreases with decreasing S_w, as is the case in the classic relative permeability functions (e.g., Brooks & Corey, 1964; Mualem, 1976). Evidently, this saturation- and frequency-dependent behavior also affects $\hat{Q}_\nu^{\text{REV}}$ and C_{EK} at the REV scale. Note that, as expressed in equation (26), $C_{EK}(S_w, \omega)$ depends on $\kappa^{\text{eff}}(S_w, \omega)$ (equation 22), which includes both the effects of $\kappa(\omega)$ (equation 5) and $\kappa^{\text{rel}}(S_w, \omega)$ (equation 19).

Figures 2d, 2e, and 2f, illustrate the frequency dependence of the absolute value of the effective excess charge density $|\hat{Q}_\nu^{\text{REV}}(S_w, \omega)|$ at different effective saturation states (equation 24). The parameters of the PSDs and the physical properties of the wetting

Table 1. Fluid properties employed in this study.

Definition	Variable	Value	Units
Fluid shear viscosity (wetting phase)	η_w	1×10^{-3}	Pa.s
Fluid density (wetting phase)	ρ_w	1000	kg/m^3
Interfacial tension (water-air)	γ	72×10^{-3}	N/m
Contact angle	β	0	rad
Dielectric permittivity of vacuum	ε_0	8.854×10^{-12}	F/m
Relative permittivity of the fluid	ε_r	80.1	-
Boltzmann constant	k_B	1.381×10^{-23}	J/K
Avogadro number	N_A	6.022×10^{23}	1/Mol
Elementary charge	e_0	1.6×10^{-19}	C
Ionic concentration	C^w_{NaCl}	10^{-4}	Mol/L
Temperature	T	293.15	K

fluid are the same as those employed in panels 2a-2c of the corresponding figure. We observe that $|\hat{Q}_\nu^{\mathrm{REV}}(S_w, \omega)|$ increases with f for $f > f_c$ irrespective of the saturation. (Jougnot & Solazzi, 2021) explored the behavior of $\hat{Q}_\nu(\omega)$ in fully saturated conditions, and observed a corresponding increase for $f > f_c$. By comparing panels 2a to 2c with panels 2d to 2f, we observe identical shifts in the characteristic frequency $f_c(S_w)$, which moves towards higher frequencies for decreasing saturation. Again, this f_c-shift is different for each PSD, evidencing larger change of f_c with saturation for the fractal PSD than for the double lognormal PSD. Note that, as shown in previous works in fully saturated media (e.g., Jougnot & Solazzi, 2021; Guarracino & Jougnot, 2018; Soldi et al., 2019), the magnitude of the effective excess charge density increases when the characteristic capillary size decreases. Consequently, the magnitude of $\hat{Q}_\nu^{\mathrm{REV}}(S_w, \omega)$ increases with decreasing S_w, as water retreats towards relatively small pores. Both the fractal and the lognormal distribution characteristics, as considered in this section, present a larger number of small pores when compared with the double lognormal PSD. This is precisely the reason for a larger relative variation in $\hat{Q}_\nu^{\mathrm{REV}}(S_w, \omega)$ values for the fractal and lognormal PSDs for decreasing saturations as compared with those associated with the double lognormal PSD.

Finally, using equations (21) to (27), we predict the frequency dependence of the electrokinetic coupling coefficient C_{EK} at different saturation states (Figs 2g, 2h, and 2i). We consider the previously described PSDs and pore fluid properties, together with representative values of $\sigma_s = 3 \times 10^{-3}$ S/m, $S_{wr} = 0.2$, $n = 1.7$ and $F = 5$ to model the variation of electrical conductivity of porous media as a function of water saturation S_w. To infer the electrical conductivity σ_w from C^w, we employ the relation $\sigma_w = 10\times C^w$ for a NaCl solution (Sen & Goode, 1992). The results show that the magnitude of C_{EK} decreases with increasing frequency for $f > f_c$ irrespective of S_w (Figs 2g, 2h, and 2i). This behavior is in good match with published works for the case of full saturation (e.g., Jougnot & Solazzi, 2021; Pride, 1994; Revil & Mahardika, 2013). Even though the amplitude of C_{EK} appears to decrease with decreasing S_w for lognormal (Fig. 2h) and double lognormal PSDs (Fig. 2i), this is not the case for the fractal PSD (Fig. 2g). In the latter case, we note that the amplitude of C_{EK} increases and, then, decreases with saturation, a behavior that is more clearly illustrated below (Figure 3).

For completeness, we illustrate the behavior of κ_w^{eff}, $\hat{Q}_\nu^{\text{REV}}$, and C_{EK} as functions of the effective saturation S_{we}, for different frequencies (Figure 3). Black circled lines denote the so-called low frequency limit for κ^{eff}, $\hat{Q}_\nu^{\text{REV}}$, and C_{EK}, while colored lines depict the responses for $f = 10^2$ Hz, $f = 10^3$ Hz, and $f = 10^4$ Hz. We observe that all curves tend to the same value for sufficiently small S_{we} values, irrespective of the probing frequency. This is expected, as f_c shifts towards higher frequencies for decreasing saturations (see Figure 2). Hence, the probing frequencies became smaller than f_c for sufficiently low saturations and κ_w^{eff}, $\hat{Q}_\nu^{\text{REV}}$, and C_{EK} tend to their low-frequency counterparts. Conversely, for increasing S_{we}, the overall responses experience a departure from the low-frequency behavior. Figure 3 evidences the control that the PSD has on $\kappa_w^{\text{eff}}(S_w)$, $\hat{Q}_\nu^{\text{REV}}(S_w)$, and $C_{\text{EK}}(S_w)$ for different probing frequencies, as we note different slopes and inflections for different PSDs.

4 Discussion

In this section, we compare the $\hat{Q}_\nu^{\text{REV}}(\omega, S_w)$ estimates obtained by means of the proposed flux-averaging approach with respect to those predicted by the pioneering model of Revil and Mahardika (2013). Then, we address the capability of the proposed model to predict experimental measurements of $C_{EK}^{rel}(\omega, S_w)$ which, to date, have been only performed under fully saturated conditions ($S_w = 1$).

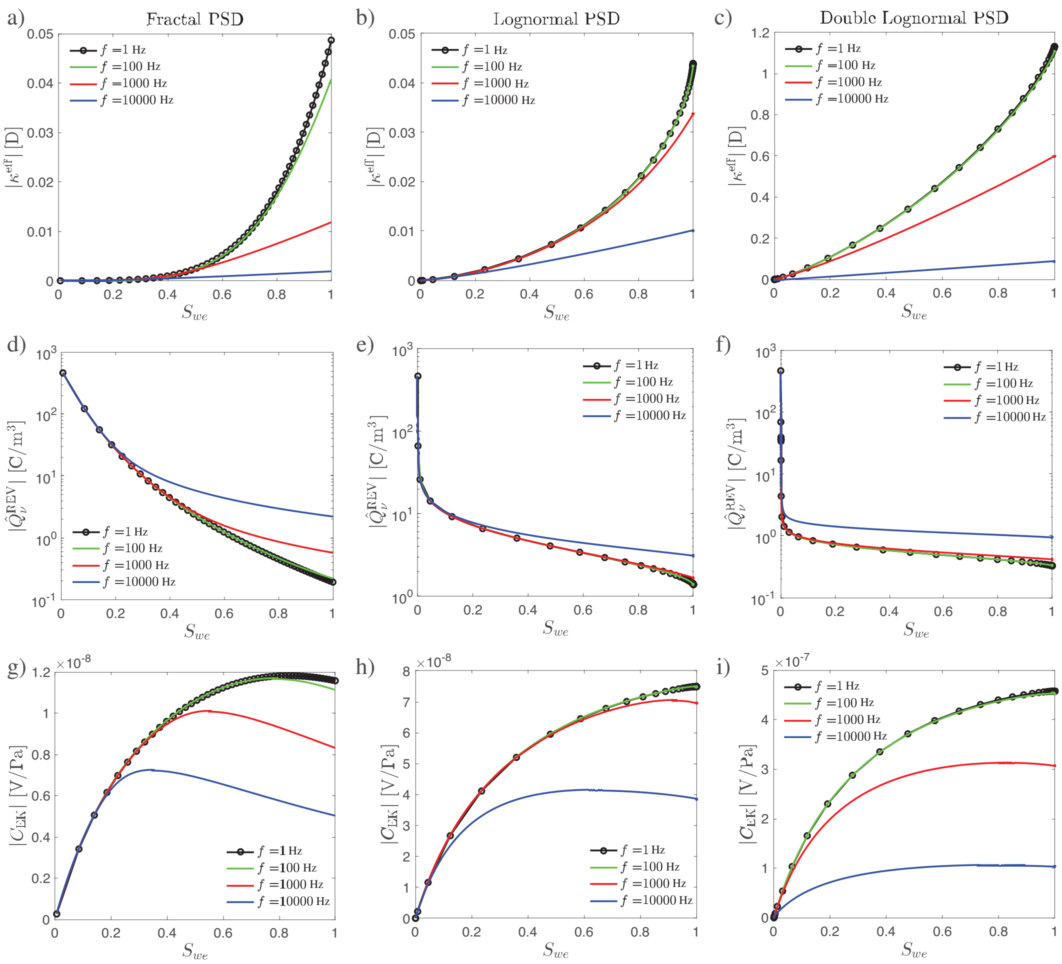

Figure 3. Absolute value of the effective dynamic permeability κ_w^{eff}, effective excess charge density $\hat{Q}_\nu^{\text{REV}}$, and effective electrokinetic coupling coefficient C_{EK} as functions of saturation for different frequencies. Each row illustrates the result for a different PSD: (a, d, g) fractal ($D = 1.5$); (b, e, h) lognormal ($R^* = 10\,\mu\text{m}$ and $\mathfrak{s} = 0.46$); and (c, f, i) double lognormal ($R_1^* = 3.1\,\mu\text{m}$, $R_2^* = 31\,\mu\text{m}$, $\mathfrak{s}_d = \mathfrak{s}/2$, $\beta_1 = 0.09$, and $\beta_2 = 0.91$).

4.1 Comparison with Previous Models

In their classical work, Revil and Mahardika (2013) proposed the following empirical model for the frequency- and saturation-dependent effective excess charge density

$$\hat{Q}_\nu^{\mathrm{REV}}(S_w, \omega) \simeq \hat{Q}_\nu^0(S_w)\sqrt{1 - i\omega\tau_k\left(S_w\right)}, \tag{36}$$

where $\hat{Q}_\nu^0(S_w)$ denotes the low-frequency value of the effective excess charge density and τ_k denotes the relaxation time of the frequency-dependent behavior, which is given by

$$\tau_k(S_w) = \kappa^{\mathrm{eff}}(S_w)\frac{\rho_w F S_w^{1-n}}{\eta_w}. \tag{37}$$

In order to compute equation (36) , Revil and Mahardika (2013) use the volume averaging model of Linde et al. (2007)

$$\hat{Q}_\nu^0(S_w) \simeq \frac{\hat{Q}_\nu^{\mathrm{sat},\,0}}{S_w}. \tag{38}$$

where $\hat{Q}_\nu^{\mathrm{sat},\,0}$ is the low-frequency effective excess charge density in fully saturated conditions. To estimate $\kappa^{\mathrm{eff}}(S_w)$, the authors take the Brooks and Corey (1964) model

$$\kappa^{\mathrm{eff}}(S_w) = \kappa_0 S_w^{\frac{2+3\lambda}{\lambda}}, \tag{39}$$

with λ a fitting parameter that is determined by the pore space characteristics of the probed medium.

It is important to remark that equation (36) is based on a linear and low-frequency approximation of the dynamic permeability, which is commonly used to deal with $\kappa(\omega)$ in the space-time domain (e.g., Revil & Mahardika, 2013). Given that the proposed flux-averaging approach (equation 24) is developed in the space-frequency domain, our estimates are not limited by such assumption. More importantly, in equation (36), Revil and Mahardika (2013) assume that equations (38) and (39) hold for the probed medium. If we wish to compare our approach with such model, it is important to analyze first the validity of equations (38) and (39) for the considered PSDs.

Figure 4 shows a comparison between equations (38) and (39) with the corresponding ones considered in this work, which respond to equations (6) and (24) (in the low frequency). We observe that equation (39) correctly reproduces the tendencies of the effective permeability associated with the fractal PSD (Figure 4a), which is in agreement with the observations of Soldi et al. (2017) for fractal media. Considering typical λ values, we note that equation (39) tends to underestimate $\kappa^{\mathrm{eff},0}(S_w)$ for lognormal and double lognormal PSDs (Figures 4b and 4c). We remark that the considered pore-structure

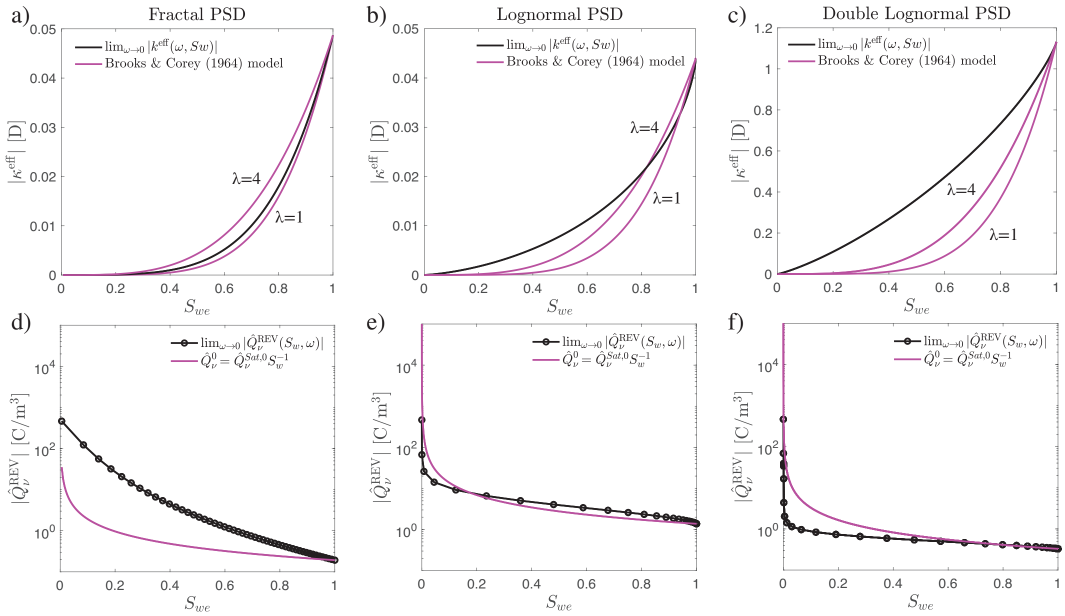

Figure 4. (a, b, c) Effective permeability and effective excess charge density as a function of the effective saturation in the low-frequency limit for: (a, d) fractal ($D = 1.8$, $R_{\min} = 23$ nm and $R_{\max} = 4.7$ μm), (b, e) lognormal ($R^* = 1.4$μm and $\mathfrak{s} = 0.15$), and (c, d) double lognormal ($R_1^* = 1.0\,\mu$m, $R_2^* = 1.5\,\mu$m, $\mathfrak{s}_d = \mathfrak{s}/2$, $\beta_1 = 0.4$, and $\beta_2 = 0.6$) PSDs. Panels (a, b, c) illustrate the behavior of equation (39) for $\lambda = \{1, 4\}$ (magenta solid lines) and that of equation (6) (black circled lines). Panels (d, e, c) illustrate the behavior predicted by equation (38) (magenta solid lines) compared with that of (24) in the low-frequency range (black circled lines).

is highly idealized and these differences can be a source of mismatch, as equation (39) is known to provide reliable predictions of $\kappa^{\text{eff},0}(S_w)$ in siliciclastic rocks. On the other hand, Figures 4d to 4f allow us to test the assumption expressed in equation (38). Interestingly, we note that this equation provides with a fair representation of $\lim_{\omega\to 0}|\hat{Q}_\nu^{\text{REV}}|$ when considering a lognormal PSD. However, it tends to give biased representations of the corresponding variable for fractal and double lognormal PSDs. Particularly, equation (38) results in estimations that significantly differ from those predicted by the low-frequency limit of equation (24) for low saturations. We conclude that, when comparing the proposed approach with that of Revil and Mahardika (2013) (equation 36), differences associated with the estimates given by equations (38) and (39) may be a source of mismatch. In order to circumvent this issue and, also, given that performing low-frequency measurements of $\kappa^{\text{eff},0}(S_w)$ and $\hat{Q}_\nu^{\text{REV},0}(S_w)$ is feasible in laboratory setups, in the following, we propose to perform the comparison of equations (24) and (36) assuming that $\kappa^{\text{eff},0}(S_w)$ and $\hat{Q}_\nu^{\text{REV},0}(S_w)$ are known and, in this case, given by those resulting from the flux-averaging approach proposed in this work. As such, below, we concentrate solely on comparing the frequency-dependent response predicted by our model and that of Revil and Mahardika (2013).

Figure 5 shows a comparison between the results from equation (24) (solid lines) and (36) (dashed lines) for the proposed PSDs, at each column. The first row depicts the absolute value of $|\hat{Q}_\nu^{\text{REV}}(S_w,\omega)|$ as a function of frequency (for different saturation states) and the second row the corresponding behavior as a function of saturation (for different probing frequencies). We observe that, in general, the proposed flux-averaging model and the model of Revil and Mahardika (2013) provide with similar tendencies. In particular, estimates are largely similar for saturations approaching unity (Figures 5a to 5c) and at relatively low frequencies (Figures 5d to 5f). Given that the proposed model obtained the corresponding estimates, for the first time in the literature, averaging the physical processes from the pore to the REV scale, we are thus validating the model of Revil and Mahardika (2013) and proving its consistency and robustness despite its simplicity.

4.2 Comparison with Experimental Data

To date, measurements of $C_{EK}^{rel}(\omega)$ for different probing frequencies have been performed only under fully saturated conditions. The proposed model should have the ca-

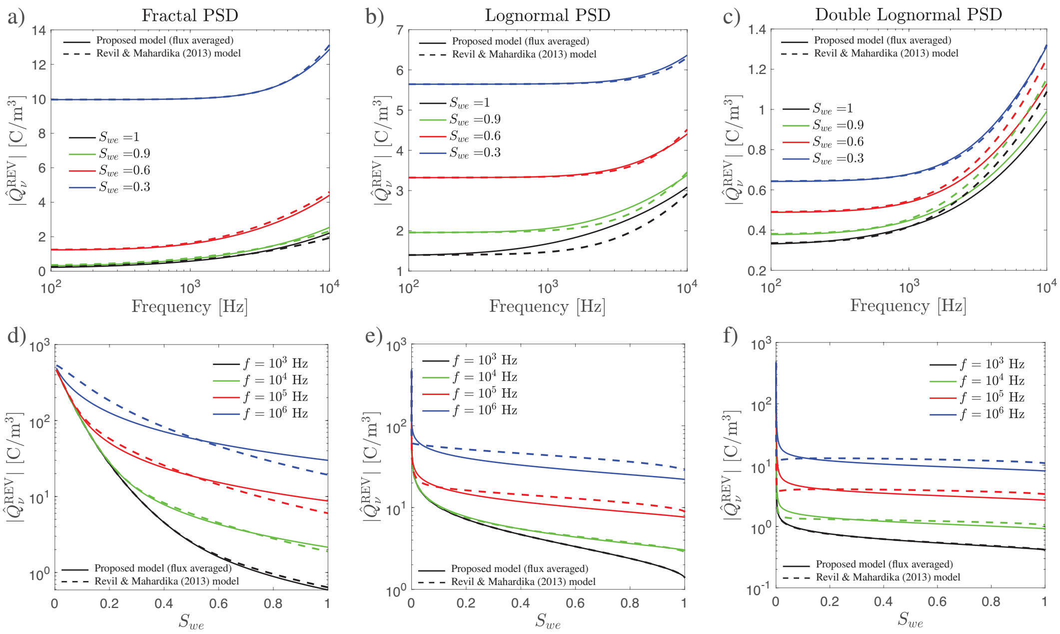

Figure 5. Effective excess charge density as a function of (a, b, c) frequency and (d, e, f) of the effective saturation. We consider: (a, d) a fractal PSD ($D = 1.8$, $R_{\min} = 23\,\mu$m and $R_{\max} = 4.7\,\mu$m, $m = 1.19$); (b, e) a lognormal PSD ($R^* = 1.4\mu$m and $\mathfrak{s} = 0.15$, $m = 1.06$), and (c, d) a double lognormal PSD ($R_1^* = 1.0\,\mu$m, $R_2^* = 1.5\,\mu$m, $\mathfrak{s}_d = \mathfrak{s}/2$, $\beta_1 = 0.4$, and $\beta_2 = 0.6$, $m = 1$) PSDs. Solid lines illustrate the behavior of the proposed flux-averaging model (equation 24) and dashed lines illustrate the behavior predicted by Revil and Mahardika (2013) model (equation 36).

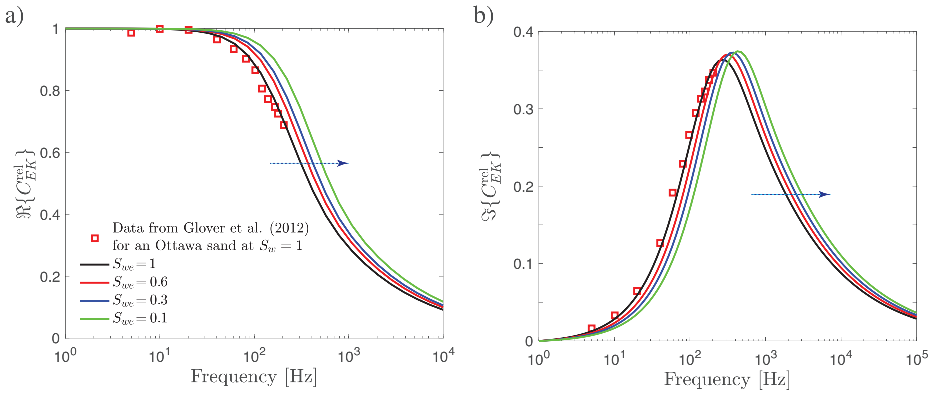

Figure 6. (a) Real and (b) imaginary parts of the relative electrokinetic coupling coefficient as functions of frequency. We illustrate results of the proposed model for different saturations (solid lines) using a lognormal PSD. Red squares depict the experimental measurements of Glover, Walker, and Jackson (2012) for an Ottawa sand at full saturation. We also illustrate the predictions of the proposed model for other saturations (colored lines). The dashed blue arrows indicate the direction in which saturation decreases.

pability of representing experimental measurements in such end-member scenario of saturation and, also, to predict the partially saturated response of the corresponding media.

Figure 6 shows the frequency dependence of the real and imaginary parts of $C_{EK}^{rel}(\omega)$ at fully saturated conditions as reported by Glover, Walker, Ruel, and Tardif (2012) for an Ottawa sand sample. The Ottawa sand is characterized by a mean grain radius of 235 µm. Glover, Walker, Ruel, and Tardif (2012) used a 10^{-3} mol/L NaCl electrolyte. We employed a lognormal PSD in combination with equation (17), that is equation (28) with S_w=1, to model the behavior of the measured data. We take $R_{min} = 1.05\,\mu$m and $R_{min} = 105\,\mu$m, as well as $R^* = 60$ µm and $s = 0.15$. Note that R^* is close to the effective pore radii of $r_p = 67$ µm, as reported by Glover, Walker, Ruel, and Tardif (2012) for the corresponding sample. The pore fluid properties are summarized in Table 1. We observe that the proposed model is able to reproduce experimental data (Figure 6, black lines). We also illustrate variations predicted by the proposed model for C_{EK}^{rel} for saturations of $S_w = 0.6$, 0.3 and 0.1 (Figure 6, colored lines). The dashed blue arrows indicate the direction in which saturation decreases in Figures 6a and 6b, evidencing an increase of

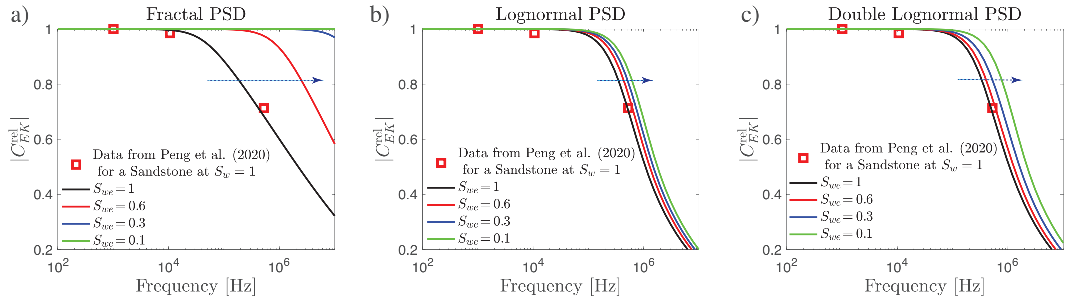

Figure 7. Amplitude of the electrokinetic coupling coefficient as function of frequency for different saturations. Each column displays the results for a different PSDs: (a) fractal ($D = 1.8$, $R_{\min} = 23$ nm and $R_{\max} = 4.7$ µm), (b) lognormal ($R^* = 1.4$µm and $\mathfrak{s} = 0.15$), and (c) double lognormal ($R_1^* = 1.0$ µm, $R_2^* = 1.5$ µm, $\mathfrak{s}_d = \mathfrak{s}/2$, $\beta_1 = 0.4$, and $\beta_2 = 0.6$). Red squares depict the experimental measurements of Peng et al. (2020) for a fully saturated sandstone. We also illustrate the predictions of the proposed model for other saturations (colored lines). The dotted blue arrows indicate the direction in which saturation decreases.

f_c with decreasing S_w, a fact that is also observed in the effective permeability curves for lognormal distributions (Figure 2b).

Figures 7 shows the frequency dependence of $|C_{EK}^{rel}|$ at full saturation for a sandstone sample, as measured by Peng et al. (2020) (red squares). We show that the proposed model is capable of fitting the main trend of experimental data by means of the three PSD described in this study, by using: (a) fractal ($D = 1.8$, $R_{\min} = 23$ nm and $R_{\max} = 4.7$ µm), (b) lognormal ($R^* = 1.4$µm and $\mathfrak{s} = 0.15$), and (c) double lognormal ($R_1^* = 1.0$ µm, $R_2^* = 1.5$ µm, $\mathfrak{s}_d = \mathfrak{s}/2$, $\beta_1 = 0.4$, and $\beta_2 = 0.6$). We remark that, because of computational restrictions involved with the numerical integrations performed in this work, we do not carry out a full inversion of the parameters but empirically find those which provide a relatively good fit with experimental data. Nevertheless, these parameters are similar to those reported by Thanh et al. (2021) for the same sample to model the frequency dependence of the electrokinetic coupling coefficient, that is directly expressed via the Zeta potential rather than the effective excess charge density. Once again, we illustrate the predicted variations of $|C_{EK}^{rel}|$ for different saturations (colored lines).

Finally, Figure 8 shows the frequency dependence of $|C_{EK}|$ measured by Zhu and Toksoz (2013) for a sample of Berea sandstone (squared curves) for different electrical conductivities. We employ the proposed model considering $R_{\min} = 0.13\,\mu$m and $R_{\max} =$

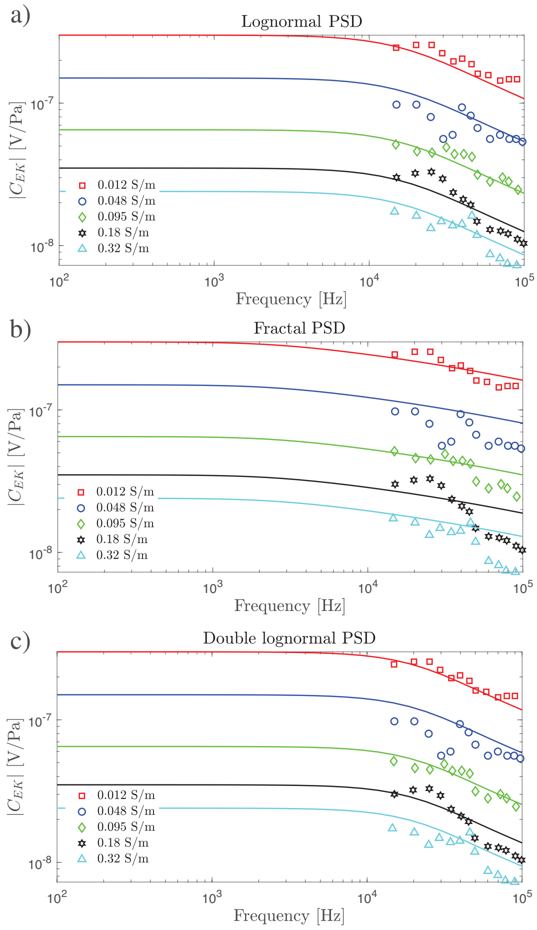

Figure 8. Amplitude of the electrokinetic coupling coefficient as functions of frequency under saturated conditions for different electrical conductivities. Colored squares denote measurements taken by Zhu and Toksoz (2013) for a Berea sandstone. We illustrate the predictions of the proposed model for three different PSDs: (a) fractal ($D = 1.65$, $R_{\min} = 0.13$ µm and $R_{\max} = 30$ µm), (b) lognormal ($R^* = 6.3$ µm and $\mathfrak{s} = 0.15$, $R_{\min} = 0.13$ µm and $R_{\max} = 30$ µm), and (c) double lognormal ($R_1^* = 1.0$ µm, $R_2^* = 3.0$ µm, $\mathfrak{s}_d = \mathfrak{s}/2$, $\beta_1 = 0.4$, and $\beta_2 = 0.6$).

30 μm for the different PSD (see solid lines), that is, (a) fractal ($D = 1.65$), (b) lognormal ($R^* = 6.3$µm and $\mathfrak{s} = 0.15$) and (c) double lognormal ($R_1^* = 1.0$ µm, $R_2^* = 3.0$ µm, $\mathfrak{s}_d = \mathfrak{s}/2$, $\beta_1 = 0.4$, and $\beta_2 = 0.6$). The values of C_{EK}^0 are reported to be 0.3×10^{-6}, 0.15×10^{-6}, 0.065×10^{-6}, 0.035×10^{-6} and 0.024×10^{-6} V/Pa for 0.012, 0.048, 0.095, 0.18 and 0.32 S/m, respectively (Zhu & Toksoz, 2013). Using equation (17), we are able to obtain C_{EK}^{rel} and, hence, C_{EK}. It is seen that the proposed approach using three considered PSDs is capable of reproducing the experimental data very well.

5 Conclusions

We proposed a flux averaging approach to compute the frequency- and saturation-dependent effective excess charge density in partially saturated porous media. For this, we conceptualized the pore space as a bundle of capillary tubes with a given pore size distribution (PSD). We modeled the frequency dependence of the effective excess charge density by solving the Navier-Stokes equations under oscillatory flow conditions within the capillaries that are effectively saturated for a given capillary pressure state. Overall, we derived expressions for: (i) the capillary pressure–saturation relationship of the probed medium; and for the saturation- and frequency-dependent (ii) effective permeability $\kappa^{\text{eff}}(S_w, \omega)$, (iii) effective excess charge density $\hat{Q}_\nu^{REV}(S_w, \omega)$, and (iv) electrokinetic coupling coefficient $C_{\text{EK}}(S_w, \omega)$.

The variation of κ^{eff}, $\hat{Q}_\nu^{\text{REV}}$ and C_{EK} with frequency at different saturation states are analyzed and explained for three different PSDs (fractal, lognormal and double lognormal PSDs). It is shown that the PSD has strong effect on the critical frequency ω_{c} and the characteristics of κ^{eff}, $\hat{Q}_\nu^{\text{REV}}$ and C_{EK} as functions of frequency and saturation. Namely, the critical frequency ω_{c} increases with decreasing water saturation S_w for a given PSD. The reason is that when the water saturation decreases, only the smaller radius pores are saturated by water, leading to a decrease of the characteristic radius representative $\tilde{R}$ of the saturated pores. This process affects the effective excess charge density at the REV scale. The proposed model is compared with previous models in the literature and, in the case of full saturation, it is also compared with published data. We found that the proposed model is capable of reproducing the frequency-dependence of $\hat{Q}_\nu^{\text{REV}}$ as predicted by previous models, which do not rely in a flux-averaging approach, provided that the low-frequency estimates of the effective excess charge and effective permeability are correct. On the other hand, our approach was able to represent experimental measurements of the coupling coefficient C_{EK} for different frequencies, conductivities, and rock properties. The proposed approach is valid for practically any PSD and constitutes a practical framework for the interpretation of seismoelectric signatures of partially saturated media.

Data Availability Statement

The data and computational codes associated with this paper are available online from https://doi.org/10.5281/zenodo.6620462.

Acknowledgments

L. D. T thanks the Vietnam National Foundation for Science and Technology Development (NAFOSTED), grant number 103.99-2019.316. D. J. acknowledge the support of the GeoProcesS project funded by the Emergence(s) Ville de Paris program. K. H. thanks the support from the National Natural Science Foundation of China under Grant 42104069.

References

Auriault, J.-L., Borne, L., & Chambon, R. (1985). Dynamics of porous saturated media, checking of the generalized law of Darcy. *J. Acoust. Soc. Am.*, *77*(5), 1641–1650.

Bear, J. (1972). *Dynamics of Fluids in Porous Media.* N. Y.: Elsevier.

Blunt, M. J. (2017). *Multiphase Flow in Permeable Media: A Pore-Scale Perspective.* Cambridge University Press.

Bordes, C., Sénéchal, P., Barrière, J., Brito, D., Normandin, E., & Jougnot, D. (2015). Impact of water saturation on seismoelectric transfer functions: a laboratory study of coseismic phenomenon. *Geophys. J. Int.*, *200*(3), 1317-1335.

Brooks, R., & Corey, A. (1964). *Hydraulic properties of porous media.* Colorado State University.

Butler, K. E. (1996). *Seismoelectric effects of electrokinetic origin.* PhD thesis, University of British Columbia.

Collini, H., & Jackson, M. D. (2022). Relationship between zeta potential and wettability in porous media: insights from a simple bundle of capillary tubes model. *J. Colloid Interface Sci.*, *608*, 605–621.

Dupuis, J. C., Butler, K. E., & Kepic, A. W. (2007). Seismoelectric imaging of the vadose zone of a sand aquifer. *Geophysics*, *72*(6), A81–A85.

Gao, Y., Harris, J. M., Wen, J., Huang, Y., Twardzik, C., Chen, X., & Hu, H. (2016). Modeling of the coseismic electromagnetic fields observed during the 2004 Mw 6.0 Parkfield earthquake. *Geophys. Res. Lett.*, *43*(2), 620–627.

Garambois, S., & Dietrich, M. (2001). Seismoelectric wave conversions in porous media: Field measurements and transfer function analysis. *Geophysics*, *66*(5), 1417–1430.

Glover, P. W. J., Walker, E., & Jackson, M. (2012). Streaming-potential coefficient of reservoir rock: A theoretical model. *Geophysics*, *77(2)*(2), D17-D43.

Glover, P. W. J., Walker, E., Ruel, J., & Tardif, E. (2012). Frequency-dependent streaming potential of porous media-part 2: Experimental measurement of unconsolidated materials. *Int. J. Geophys.*, *2012*.

Grobbe, N., Revil, A., Zhu, Z., & Slob, E. (2020). *Seismoelectric exploration: Theory, experiments, and applications* (Vol. 252). John Wiley & Sons.

Guarracino, L., & Jougnot, D. (2018). A physically based analytical model to describe effective excess charge for streaming potential generation in water saturated porous media. *J. Geophys. Res.: Solid Earth*, *123*(1), 52-65.

Guarracino, L., Rötting, T., & Carrera, J. (2014). A fractal model to describe the evolution of multiphase flow properties during mineral dissolution. *Adv Water Resour*, *67*, 78–86.

Han, S.-J., Kim, S.-S., & Kim, B.-I. (2004). Electroosmosis and pore pressure development characteristics in lead contaminated soil during electrokinetic remediation. *Geosci. J.*, *8*(1), 85–93.

Jaafar, M. Z., Vinogradov, J., & Jackson, M. D. (2009). Measurement of streaming potential coupling coefficient in sandstones saturated with high salinity nacl brine. *Geophys. Res. Lett.*, *36*(L21306), doi:10.1029/2009GL040549.

Jackson, M. D. (2010). Multiphase electrokinetic coupling: Insights into the impact of fluid and charge distribution at the pore scale from a bundle of capillary tubes model. *J. Geophys. Res.: Solid Earth*, *115*(B7).

Johnson, D. L., Koplik, J., & Dashen, R. (1987). Theory of dynamic permeability and tortuosity in fluid-saturated porous media. *J. Fluid Mech.*, *176*, 379-402. doi: 10.1017/S0022112087000727

Jougnot, D., Linde, N., Revil, A., & Doussan, C. (2012). Derivation of soil-specific streaming potential electrical parameters from hydrodynamic characteristics of partially saturated soils. *Vadose Zone J.*, *11*(1), 272-286.

Jougnot, D., Mendieta, A., Leroy, P., & Maineult, A. (2019). Exploring the effect of the pore size distribution on the streaming potential generation in saturated porous media, insight from pore network simulations. *J. Geophys. Res.: Solid*

Earth, *124*(6), 5315–5335.

Jougnot, D., Revil, A., Ghorbani, A., Leroy, P., & Cosenza, P. (2010). Spectral induced polarization of partially saturated clay-rocks: a mechanistic approach. *Geophys. J. Int.*, *180*(1), 210-224.

Jougnot, D., Roubinet, D., Guarracino, L., & Maineult, A. (2020). Modeling streaming potential in porous and fractured media, description and benefits of the effective excess charge density approach. In *Advances in Modeling and Interpretation in Near Surface Geophysics* (pp. 61–96). Springer.

Jougnot, D., Rubino, J. G., Carbajal, M. R., Linde, N., & Holliger, K. (2013). Seismoelectric effects due to mesoscopic heterogeneities. *Geophys. Res. Lett.*, *40*(10), 2033–2037.

Jougnot, D., & Solazzi, S. G. (2021). Predicting the frequency-dependent effective excess charge density: A new up-scaling approach for seismoelectric modelling. *Geophysics*, *86*(3), 1-10.

Kozeny, J. (1927). Über kapillare Leitung des Wassers im Boden. *Akad. Wiss*, *136(2a)*, 271–306.

Li, J. X., Rezaee, R., & Müller, T. M. (2020). Wettability effect on wave propagation in saturated porous medium. *J. Acoust. Soc*, *147*(2), 911–920.

Li, J. X., Rezaee, R., Müller, T. M., & Sarmadivaleh, M. (2021). Pore size distribution controls dynamic permeability. *Geophys. Res. Lett.*, *48*(5), e2020GL090558.

Linde, N., Jougnot, D., Revil, A., Matthäi, S., Arora, T., Renard, D., & Doussan, C. (2007). Streaming current generation in two-phase flow conditions. *Geophys. Res. Lett.*, *34*(3).

Mavko, G., Mukerji, T., & Dvorkin, J. (2009). *The rock physics handbook: Tools for seismic analysis of porous media.* Cambridge University Press.

Monachesi, L. B., Zyserman, F. I., & Jouniaux, L. (2018). An analytical solution to assess the sh seismoelectric response of the vadose zone. *Geophys. J. Int.*, *213*(3), 1999–2019.

Mualem, Y. (1976). A new model for predicting the hydraulic conductivity of unsaturated porous media. *Water Resour. Res.*, *12*(3), 513–522.

Packard, R. G. (1953). Streaming potentials across glass capillaries for sinusoidal pressure. *J. Chem. Phys.*, *21*(2), 303-307.

Peng, R., Di, B., Glover, P. W. J., Wei, J., Lorinczi, P., Liu, Z., & Li, H. (2020). Seismo-electric conversion in shale: experiment and analytical modelling. *Geophys. J. Int.*, *223*(2), 725-745.

Pride, S. R. (1994). Governing equations for the coupled electromagnetics and acoustics of porous media. *Phys. Rev. B*, *50*(21), 15678.

Pride, S. R., & Morgan, F. D. (1991). Electrokinetic dissipation induced by seismic waves. *Geophysics*, *56*(7), 914-925.

Reppert, P. M. (2001). Frequency-dependent streaming potentials. *J. Colloid and Interf. Sci.*, *234*(1), 194 - 203. doi: 10.1006/jcis.2000.7294

Revil, A. (2013). Effective conductivity and permittivity of unsaturated porous materials in the frequency range 1 mHz–1GHz. *Water Resour. Res.*, *49*(1), 306-327.

Revil, A., & Jardani, A. (2010). Seismoelectric response of heavy oil reservoirs: theory and numerical modelling. *Geophys. J. Int.*, *180*(2), 781–797.

Revil, A., Jardani, A., Sava, P., & Haas, A. (2015). *The seismoelectric method: Theory and applications.* John Wiley & Sons.

Revil, A., & Mahardika, H. (2013). Coupled hydromechanical and electromagnetic disturbances in unsaturated porous materials. *Water Resour. Res.*, *49*, 744-766.

Rosas-Carbajal, M., Jougnot, D., Rubino, J. G., Monachesi, L., Linde, N., & Holliger, K. (2020). Seismoelectric signals produced by mesoscopic heterogeneities: Spectroscopic analysis of fractured media. *Seismoelectric Exploration: Theory, Experiments, and Applications*, 269–287.

Sen, P. N., & Goode, P. A. (1992). Influence of temperature on electrical conductivity on shaly sands. *Geophysics*, *57*(1), 89-96.

Smeulders, D., Eggels, R., & Van Dongen, M. (1992). Dynamic permeability: reformulation of theory and new experimental and numerical data. *J. Fluid Mech.*, *245*, 211–227.

Solazzi, S. G., Rubino, J. G., Jougnot, D., & Holliger, K. (2020). Dynamic permeability functions for partially saturated porous media. *Geophys. J. Int.*, *221*(2), 1182–1189.

Soldi, M., Guarracino, L., & Jougnot, D. (2017). A simple hysteretic constitutive model for unsaturated flow. *Transport Porous Med.*, *120*(2), 271–285.

Soldi, M., Guarracino, L., & Jougnot, D. (2019). An analytical effective excess charge density model to predict the streaming potential generated by unsaturated flow. *Geophys. J. Int.*, *216*(1), 380-394.

Thanh, L. D., Jougnot, D., Solazzi, S. G., Van Nghia, N., & Van Do, P. (2021). Dynamic streaming potential coupling coefficient in porous media with different pore size distributions. *Geophys. J. Int.*. doi: 10.1093/gji/ggab491

Thompson, A., & Gist, G. (1993). Geophysical applications of electrokinetic conversion. *Lead. Edge*, *12*(12), 1169–1173.

Tyler, S. W., & Wheatcraft, S. W. (1990). Fractal processes in soil water retention. *Water Resour. Res.*, *26*(5), 1047–1054.

Van Genuchten, M. T. (1980). A closed-form equation for predicting the hydraulic conductivity of unsaturated soils. *Soil. Sci. Soc. Am. J.*, *44*(5), 892–898.

Wang, J., Hu, H., & Guan, W. (2015). Experimental measurements of seismoelectric signals in borehole models. *Geophys. J. Int.*, *203*(3), 1937–1945.

Warden, S., Garambois, S., Jouniaux, L., Brito, D., Sailhac, P., & Bordes, C. (2013). Seismoelectric wave propagation numerical modelling in partially saturated materials. *Geophys. J. Int.*, *194*(3), 1498–1513.

Waxman, M. H., & Smits, L. (1968). Electrical conductivities in oil-bearing shaly sands. *Soc. Pet. Eng. J.*, *8*(02), 107–122.

Yu, B., Li, J., Li, Z., & Zou, M. (2003). Permeabilities of unsaturated fractal porous media. *Int. J. Multiph. Flow*, *29*(10), 1625–1642.

Zhou, M.-Y., & Sheng, P. (1989). First-principles calculations of dynamic permeability in porous media. *Phys. Rev. B*, *39*(16), 12027.

Zhu, Z., & Toksoz, M. N. (2013). Experimental measurements of the streaming potential and seismoelectric conversion in berea sandstone. *Geophys. Prospect.*, *61*, 688-700.

Zhu, Z., Toksöz, M. N., & Burns, D. R. (2008). Electroseismic and seismoelectric measurements of rock samples in a water tank. *Geophysics*, *73*(5), E153-E164. doi: 10.1190/1.2952570

Zyserman, F. I., Jouniaux, L., Warden, S., & Garambois, S. (2015). Borehole seismoelectric logging using a shear-wave source: possible application to CO_2 disposal? *Int. J. Greenh. Gas Control.*, *33*, 89–102.

Zyserman, F. I., Monachesi, L. B., & Jouniaux, L. (2017). Dependence of shear wave seismoelectrics on soil textures: a numerical study in the vadose zone. *Geophys. J. Int.*, *208*(2), 918–935.